Evaluation of and Suggested Improvements to the WSM6 Microphysics in WRF-ARW Using Synthetic and Observed *GOES-13* Imagery

LEWIS GRASSO,* DANIEL T. LINDSEY,[+] KYO-SUN SUNNY LIM,[#] ADAM CLARK,[@] DAN BIKOS,* AND SCOTT R. DEMBEK[&]

Cooperative Institute for Research in the Atmosphere, Colorado State University, Fort Collins, Colorado
[+] *NOAA/Center for Satellite Applications and Research, and Cooperative Institute for Research in the Atmosphere, Colorado State University, Fort Collins, Colorado*
[#] *Atmospheric Sciences and Global Change Division, Pacific Northwest National Laboratory, Richland, Washington*
[@] *National Severe Storms Laboratory, Norman, Oklahoma*
[&] *Cooperative Institute for Mesoscale Meteorological Studies, Norman, Oklahoma*

ABSTRACT

Synthetic satellite imagery can be employed to evaluate simulated cloud fields. Past studies have revealed that the Weather Research and Forecasting (WRF) single-moment 6-class (WSM6) microphysics scheme in the Advanced Research WRF (WRF-ARW) produces less upper-level ice clouds within synthetic images compared to observations. Synthetic *Geostationary Operational Environmental Satellite-13* (*GOES-13*) imagery at $10.7\,\mu$m of simulated cloud fields from the 4-km National Severe Storms Laboratory (NSSL) WRF-ARW is compared to observed *GOES-13* imagery. Histograms suggest that too few points contain upper-level simulated ice clouds. In particular, side-by-side examples are shown of synthetic and observed anvils. Such images illustrate the lack of anvil cloud associated with convection produced by the 4-km NSSL WRF-ARW. A vertical profile of simulated hydrometeors suggests that too much cloud water mass may be converted into graupel mass, effectively reducing the main source of ice mass in a simulated anvil. Further, excessive accretion of ice by snow removes ice from an anvil by precipitation settling. Idealized sensitivity tests reveal that a 50% reduction of the accretion rate of ice by snow results in a significant increase in anvil ice of a simulated storm. Such results provide guidance as to which conversions could be reformulated, in a more physical manner, to increase simulated ice mass in the upper troposphere.

1. Introduction

As a result of advancements in computer technology and radiative transfer physics, synthetic satellite imagery can now be generated using output from various mesoscale modeling systems. Otkin et al. (2009) conducted a Weather Research and Forecasting (WRF; Skamarock et al. 2005) simulation that covered the full disk scene of the Spinning Enhanced Visible and Infrared Imager (SEVIRI). Their simulation was configured with the Thompson microphysics scheme (Thompson et al. 2008), and synthetic SEVIRI imagery produced from a 30-h simulation showed reasonable agreement to observed SEVIRI imagery. Synthetic imagery from their study included seven individual infrared bands (IR) and some channel differences. Likewise, Grasso et al. (2010) performed a simulation of a convective event that occurred over central portions of the United States on 8 May 2003 with the Colorado State University Regional Atmospheric Modeling System (CSU-RAMS; Cotton et al. 2003). Results showed a reasonable comparison of synthetic *Geostationary Operational Environmental Satellite-12* (*GOES-12*) imagery to observed *GOES-12* imagery at both 6.5 and $10.7\,\mu$m.

In contrast to both studies outlined above, synthetic imagery at $3.9\,\mu$m is more computationally expensive. One main reason for the computational expense is the inclusion of shortwave radiation from the sun in addition to terrestrial radiation emitted from the surface and atmosphere of the earth. Grasso and Lindsey (2011) demonstrated the usefulness of synthetic *GOES-12* imagery at $3.9\,\mu$m. After comparing the appearance of simulated thunderstorm anvils in synthetic 3.9-μm imagery

Corresponding author address: Lewis Grasso, Cooperative Institute for Research in the Atmosphere, Colorado State University, Fort Collins, CO 80523-1375.
E-mail: lewis.grasso@colostate.edu

with their observed counterparts, a discrepancy in the synthetic radiance field was noticed. Their results highlighted the usefulness of synthetic imagery in finding an error with the prediction of number concentrations of pristine ice in the CSU-RAMS microphysics. One common aspect of this work and of the two listed above is the use of one microphysical scheme per study.

Like the CSU-RAMS mesoscale model, the WRF Model is also a comprehensive numerical modeling system. As such, WRF offers many microphysical schemes from which to choose for a simulation. Recent studies have begun to focus on sensitivities of simulated cloud fields to different microphysical options. For example, Jankov et al. (2011) used WRF to simulate an atmospheric river event that occurred on 30 December 2005 over western portions of California. Their simulation was repeated several times, each with a different microphysical scheme. A comparison between synthetic and observed *GOES-10* imagery at 10.7 μm showed strengths and weakness among the microphysical schemes. In particular, the Lin scheme (Lin et al. 1983; Rutledge and Hobbs 1984) produced unrealistically large amounts of ice in the upper troposphere.

A comprehensive effort to evaluate model output occurred at the Hazardous Weather Testbed, as reported by Clark et al. (2012). Many configurations of WRF were set up and run for this experiment. These included several choices of physics packages in simulations that covered the United States (Kong et al. 2007; Xue et al. 2007). As a result, copious amount of data were made available for analysis. Recently, Cintineo et al. (2014) have analyzed some of the model output during the time period from May to June of 2012. They compared synthetic and observed *GOES-13* imagery at 6.7 and 10.7 μm as a means to evaluate different surface parameterizations and different microphysical schemes. One finding focused on a noticeable reduction of the area of upper-level ice clouds in simulations that used the WRF double-moment 6-class (WDM6) microphysics scheme (Lim and Hong 2010) compared to other choices of microphysics in WRF. For completeness, WDM6 has been developed based on the WRF single-moment 6-class (WSM6) microphysics scheme (Hong and Lim 2006) by adding a double-moment treatment for the warm-rain process.

Another study also reported a reduction of upper-level ice cloud in WRF simulations that have employed the WSM6 microphysics. Van Weverberg et al. (2013) conducted simulations of mesoscale convective systems over the tropical western Pacific that occurred during the one week period from 25 December 2003 to 1 January 2004. By comparing synthetic *GOES-9* to observed *GOES-9* imagery, their Fig. 3 highlights a reduced area of simulated ice clouds when WSM6 was used. Based on their results, they suggested that enhanced evaporation of raindrops and sublimation of ice aloft might account for the reduced area of ice clouds produced by the WSM6 scheme.

Both the National Severe Storms Laboratory (NSSL) and the Storm Prediction Center (SPC) began testing the use of a convection-allowing simulation with the Advanced Research WRF (WRF-ARW) as a forecasting tool during the 2004 and 2005 National Oceanic and Atmospheric Administration (NOAA)/Hazardous Weather Testbed Spring Forecasting Experiment (Kain et al. 2006, 2010). Results from initial tests received positive feedback from forecasters. In particular, forecasters were encouraged by the ability of simulations to depict reasonable convective-scale structures associated with phenomena like mesoscale convective systems and discrete supercells. Consequently, NSSL scientists were motivated to establish a more permanent experimental modeling framework that provided storm-scale guidance to SPC forecasters. In addition, such a framework served, and still serves, as a testing ground for the development of storm-scale model diagnostics and has been known as the NSSL WRF-ARW since 2006.

Synthetic GOES-R Advanced Baseline Imager and *GOES-13* imagery have been produced at the Cooperative Institute for Research in the Atmosphere (CIRA) since 2010. Such imagery has been generated from the 4-km NSSL WRF-ARW as part of the GOES-R Proving Ground (Goodman et al. 2012). Bikos et al. (2012) discussed many forecasting applications of synthetic *GOES-13* imagery generated from the 4-km NSSL WRF-ARW. They also pointed out that simulated thunderstorm anvils in IR synthetic imagery were consistently smaller in areal extent than anvils in observed IR imagery from GOES; a result that is consistent with the findings of Van Weverberg et al. (2013).

Research reported herein is an extension of previous work by focusing specifically on the ability of the WSM6 microphysics to produce cloud ice in NSSL WRF-ARW forecasts. In an attempt to reinforce the focus of this manuscript, Fig. 5 from Bikos et al. (2012) is reproduced here as Fig. 1. As can be seen, the anvil canopy of the observed convective system existed over eastern Illinois and most of Indiana (Fig. 1b). In contrast, the simulated anvil, evident in the synthetic imagery, was underrepresented (Fig. 1a). Synthetic and observed *GOES-13* imagery are used to demonstrate seasonal discrepancies in the amount of upper level ice clouds produced by the WSM6 scheme. Proper depiction of simulated thunderstorm anvil clouds provides evidence that the model and its associated microphysical scheme are correctly distributing total water mass into the different hydrometeor species and water vapor. Additionally, simulated anvils
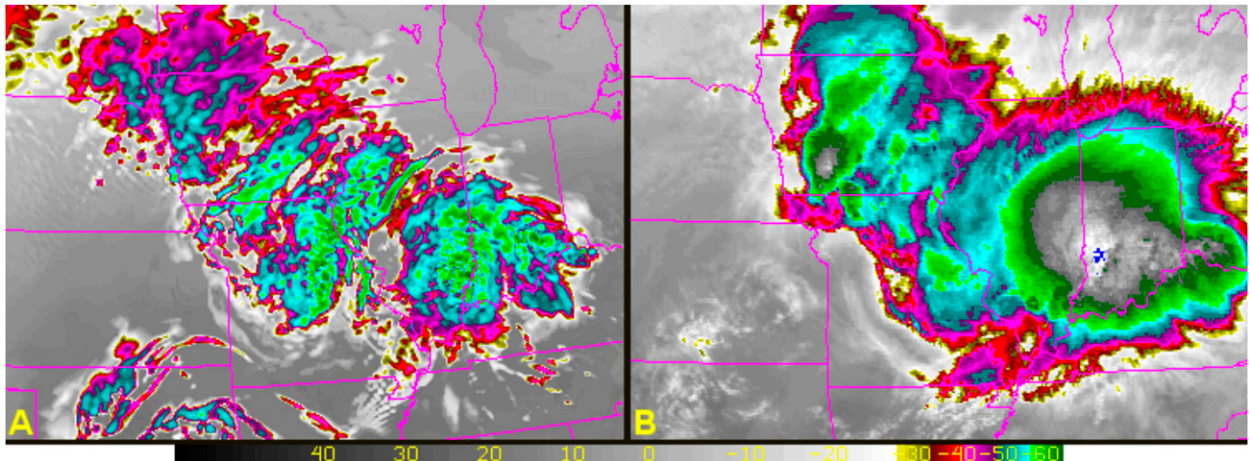
FIG. 1. (a) Synthetic GOES-R imagery at $10.35\,\mu$m from the 4-km NSSL WRF-ARW 0000 UTC 12 May 2010 model run valid at 1200 UTC. (b) Observed *GOES-13* imagery at $10.7\,\mu$m at 1232 UTC 12 May 2010. The brightness temperature scale (°C) is the same for both sets. This figure is adapted from Bikos et al. (2012).

may provide a feedback on the model's radiation scheme, resulting in more or less anvil shading, which can affect the subsequent model solution (Oberthaler and Markowski 2013).

This paper is divided into five sections. Section 2 contains a brief description of the generation of synthetic satellite imagery and the source of observed satellite imagery. Specific examples and their histograms are discussed in section 3. As a result of the findings of the statistical analysis and further diagnostics of simulated convection, a hypothesis is developed and presented, in section 4, to explain why the WSM6 scheme underrepresents ice mass in simulated anvils of thunderstorms. Following the hypothesis, WSM6 sensitivity experiments and their results are presented in section 5. Also in section 5 are suggestions to improve the ability of the WSM6 scheme to produce more ice in simulated anvils. Finally, the summary and conclusions can be found in section 6.

2. Data

Within a domain that covers the continental United States, the NSSL WRF-ARW model uses a horizontal grid spacing of 4 km in both directions. This model is run twice daily at 0000 and 1200 UTC with forecasts to 36 h. Although the configuration has remained relatively constant, two sets of upgrades have occurred to date. In June 2009, the model domain was expanded and the WRF Model version was updated from 2.1.1 to 3.1.1; in April 2013 the WRF model version was updated to 3.4.1. Physics parameterizations include the Mellor–Yamada–Janjic (Mellor and Yamada 1982) boundary layer scheme and the WSM6 microphysics scheme. Despite recent work that illustrates some advantages of using double-moment

microphysics (Jung et al. 2012; Bryan and Morrison 2012), research has yet to find quantifiable objective or subjective improvements using double-moment schemes for a 15–30-h forecast, a period in which the NSSL WRF-ARW forecasts are most heavily utilized (Clark et al. 2012, 2014). Thus, because of the computational efficiency and familiarity with SPC forecasters and other users, NSSL WRF-ARW continues to use WSM6.

For the past few years at CIRA, synthetic *GOES-13* imagery at $10.7\,\mu$m has been produced from the 0000 UTC run of the 4-km NSSL WRF-ARW. An automated system has been developed within which pressure, temperature, water vapor mixing ratio, canopy temperature, and mixing ratio values of all five habit types of the WSM6 microphysics are electronically sent to CIRA from NSSL. In addition, monthly averaged, spectrally dependent, surface emissivity (Seemann et al. 2008) values are also computed. All of these variables are necessary to calculate top-of-the-atmosphere radiance values displayed in synthetic satellite imagery. All synthetic imagery herein was generated with an observational operator that was developed at CIRA; see Grasso and Greenwald (2004), Grasso and Lindsey (2011), and Bikos et al. (2012) for model details and additional references.

Observed *GOES-13* data were acquired from an archive at CIRA. Imagery is stored in Man computer Interactive Data Access System (McIDAS) format (Lazzara et al. 1999) that is well suited for display on systems running McIDAS visualization software. A temporal frequency of 1 h was chosen as the time interval between successive images for the study herein. Both synthetic and observed data were then remapped onto the same rectilinear grid in preparation for statistical analysis.

3. Data analysis

Motivated by the observation that NSSL WRF-ARW simulated anvils are often smaller than observed anvils in IR satellite imagery (e.g., Fig. 1), additional examples were collected. Synthetic and observed *GOES-13* imagery at $10.7\,\mu\text{m}$ was remapped onto a common rectilinear grid over the same domain for comparison. A grid spacing of $0.1°$ latitude and longitude was used. Each domain was specific to the convective event, with approximately 9.0×10^4 points being used for each image. Hourly forecast times from 9 to 36 h were matched to the corresponding observed *GOES-13* times. Only observed times that occurred within 15 min of the forecast time were chosen for comparison. After the time matching, brightness temperatures (BTs) were distributed into 2-K bins and the total pixels were counted for each bin in order to generate histograms. Remapped observed and synthetic imagery are shown in Figs. 2a,b; 3a,b; and 4a,b, respectively, while the corresponding histograms appear in Figs. 2c,d; 3c,d; and 4c,d. In Figs. 2c, 3, and 4c, the histogram covers BTs from 150 to 330 K, while in Figs. 2d, 3d, and 4d the histogram is zoomed in over BTs between 190 and 250 K, representing the colder clouds.

Figure 2 shows an example of a large synoptic system affecting much of the eastern United States. Observed *GOES-13* IR imagery indicates that anvil clouds (brightness temperatures colder than approximately 220 K) extended roughly the east–west distance across Missouri and half of Illinois, and over a majority of the Mississippi River valley. In contrast, the corresponding synthetic image shows significantly warmer brightness temperatures covering a smaller east–west distance, suggesting that the NSSL WRF-ARW under-forecasted sufficiently expansive anvils near the tropopause. Associated histograms confirm that the synthetic image has more clear-sky pixels and far fewer brightness temperatures colder than 220 K. Figures 3 and 4 show additional examples of a similar model warm bias for the coldest cloud tops, including convection associated with a mesoscale system (Fig. 3) and monsoonal thunderstorm activity (Fig. 4). In both cases, the model forecasts low- and midlevel clouds (indicated by the warmer brightness temperatures) covering an area similar to the anvils in observations.

To investigate the consistency of the model's warm bias in forecast BTs for cold clouds, total histograms for the observed and synthetic imagery at $10.7\,\mu\text{m}$ were generated for the July 2011–September 2012 time period, including all 9–36-h forecasts. During that time span, the total number of points included in the histogram was approximately 8.7×10^8, while the BTs range extended from 180 to 330 K (Fig. 5a). As indicated by the histogram, too many points in the synthetic data had

brightness temperatures in the range from approximately 270 to 300 K relative to observations. Conversely, too few points in the synthetic data had BTs below about 230 K compared to observations. An enhanced view of the histogram for BTs between 190 and 250 K, representing the colder clouds, is displayed in Fig. 5b. This result confirms a lack of simulated ice clouds compared to observations.

All of the examples presented above suggest that convection in the NSSL WRF-ARW model under-forecast ice mass near the tropopause. Although other aspects of the model may contribute to this result, the WSM6 microphysics package is suspected to be the likely cause. Some possible explanations are examined in section 4. One last point concerning the use of 220 K to define an anvil is warranted. Because the edge of anvils are optically thin at $10.7\,\mu\text{m}$, some of the upwelling radiation from below will pass through observed and simulated cloud material. As a result, brightness temperatures of the edge of anvils can be warmer than 220 K. Therefore, the use of 220 K to define an anvil will likely exclude pixels associated with the edge of an anvil.

4. Hypothesis for ice loss

One advantage of synthetic satellite imagery is the ability to evaluate simulated cloud fields. As was pointed out in the introduction, Grasso and Lindsey (2011) illustrated how synthetic *GOES-12* 3.9-μm imagery was used to identify an error in the prognostic equation of pristine ice in the CSU-RAMS model. In their work, synthetic values of reflectance from anvils of simulated thunderstorms were too small compared to observations. Habit particle size was suspected to be too large, but which habit? A previous study by Grasso and Greenwald (2004) helped answer this question. They showed that the microphysical habit that radiates to space was the pristine ice field in an idealized simulation of a thunderstorm with RAMS. Their result suggested that the diameter of pristine ice in the simulated anvils in the Grasso and Lindsey (2011) study was too large.

Pristine ice in simulated anvil canopies by RAMS is generated primarily through homogeneous freezing of cloud droplets as air ascends a convective updraft. After the Grasso and Greenwald (2004) study, an upgrade occurred to the microphysics: cloud droplets changed from a single-moment habit to a two-moment habit. As a result, the conversion of cloud droplet mass to pristine ice mass exhibited continuity across the homogeneous freezing level. In contrast, a significant loss of cloud droplet numbers to pristine ice numbers occurred during the homogeneous freezing process. That is, mass was conserved during the homogeneous freezing process of
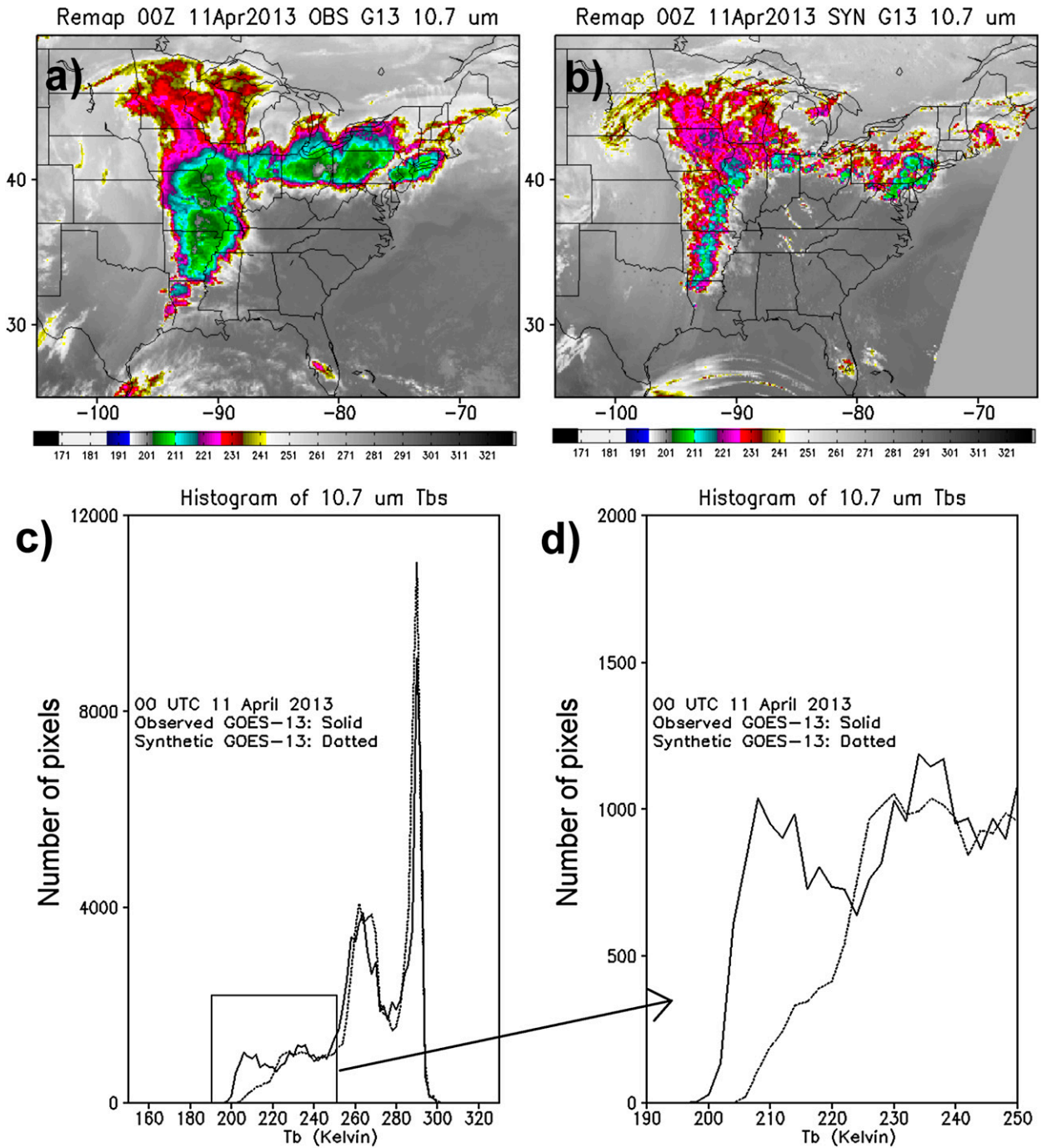
FIG. 2. (a) Observed and (b) synthetic *GOES-13* imagery at 10.7 μm valid at 0000 UTC 11 Apr 2013. Histograms of observed (solid lines) and synthetic (dashed lines) brightness temperatures corresponding to the images over (c) all brightness temperatures and (d) zoomed in the denoted box for brightness temperatures between 190 and 250 K. The synthetic image is based on a 24-h forecast from the 4-km NSSL WRF.

cloud droplets to pristine ice; number concentration was not conserved. As a result, an artificial reduction of pristine ice numbers occurred in the anvil, thus producing ice particles that were too large. Hence, the resulting reflectance values were too small. These results will be used to provide some guidance into the lack of ice within anvils of thunderstorms through the use of the WSM6 microphysics.
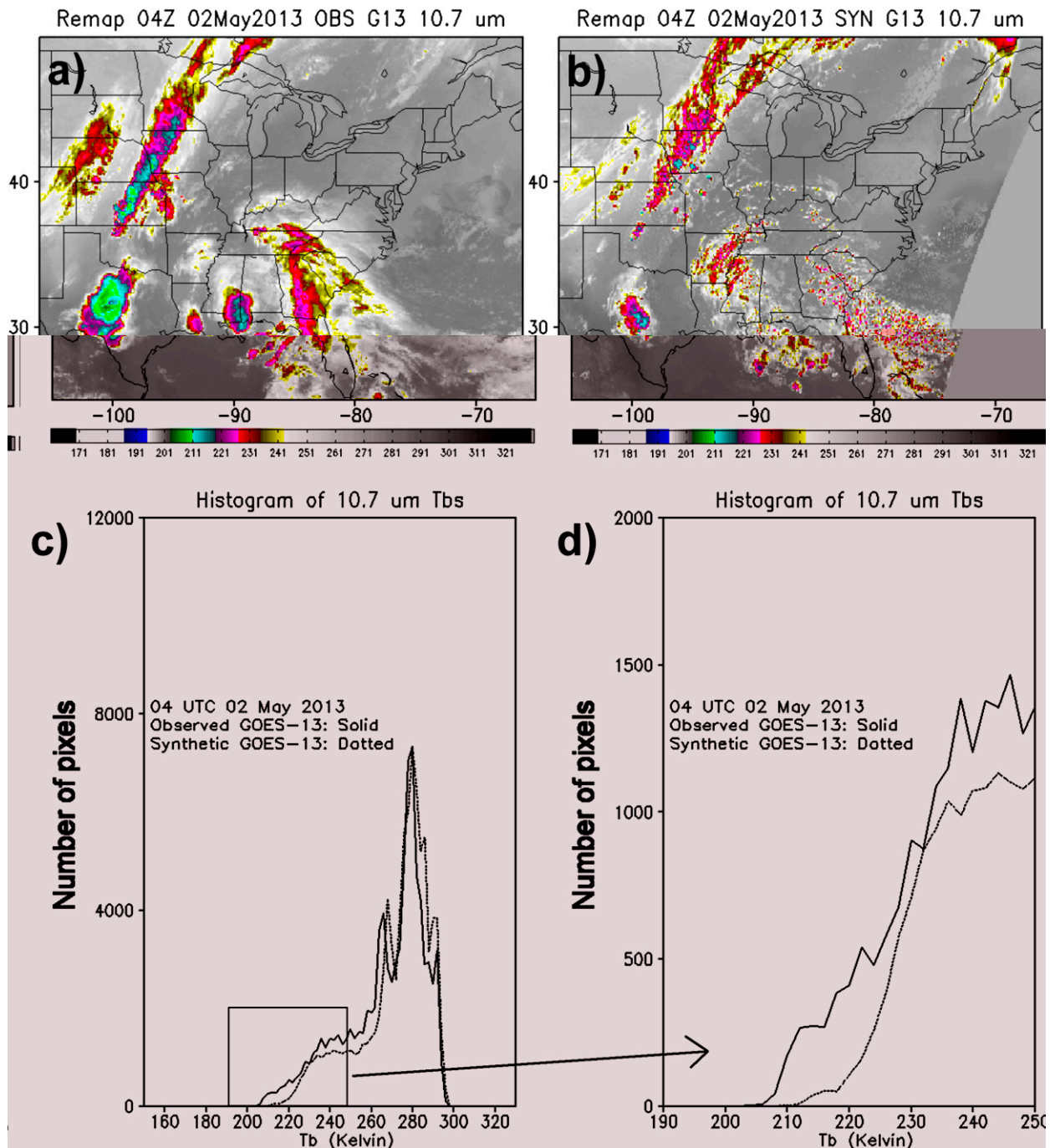
FIG. 3. As in Fig. 2, but valid at 0400 UTC 2 May 2013. The synthetic image is based on a 28-h forecast from the 4-km NSSL WRF.

Three-dimensional fields from a WRF-ARW simulation were used to highlight WSM6 microphysical habit characteristics in a convective updraft. For clarity, the five microphysical habit types are cloud droplets, rain, snow, graupel, and ice. Specifically, a simulation was extracted from the daily 4-km NSSL WRF-ARW model data that was sent to CIRA and was initialized at 0000 UTC 25 July 2013 within a domain that covered the United States. Synthetic GOES-R imagery at $10.35\ \mu m$ was produced from a 24-h forecast valid at 0000 UTC 26 July 2013 (Fig. 6a). Convection existed in the simulation over the southern Texas Panhandle at the time of the synthetic image (Fig. 6b). An X–Z vertical cross section of many model variables was produced along
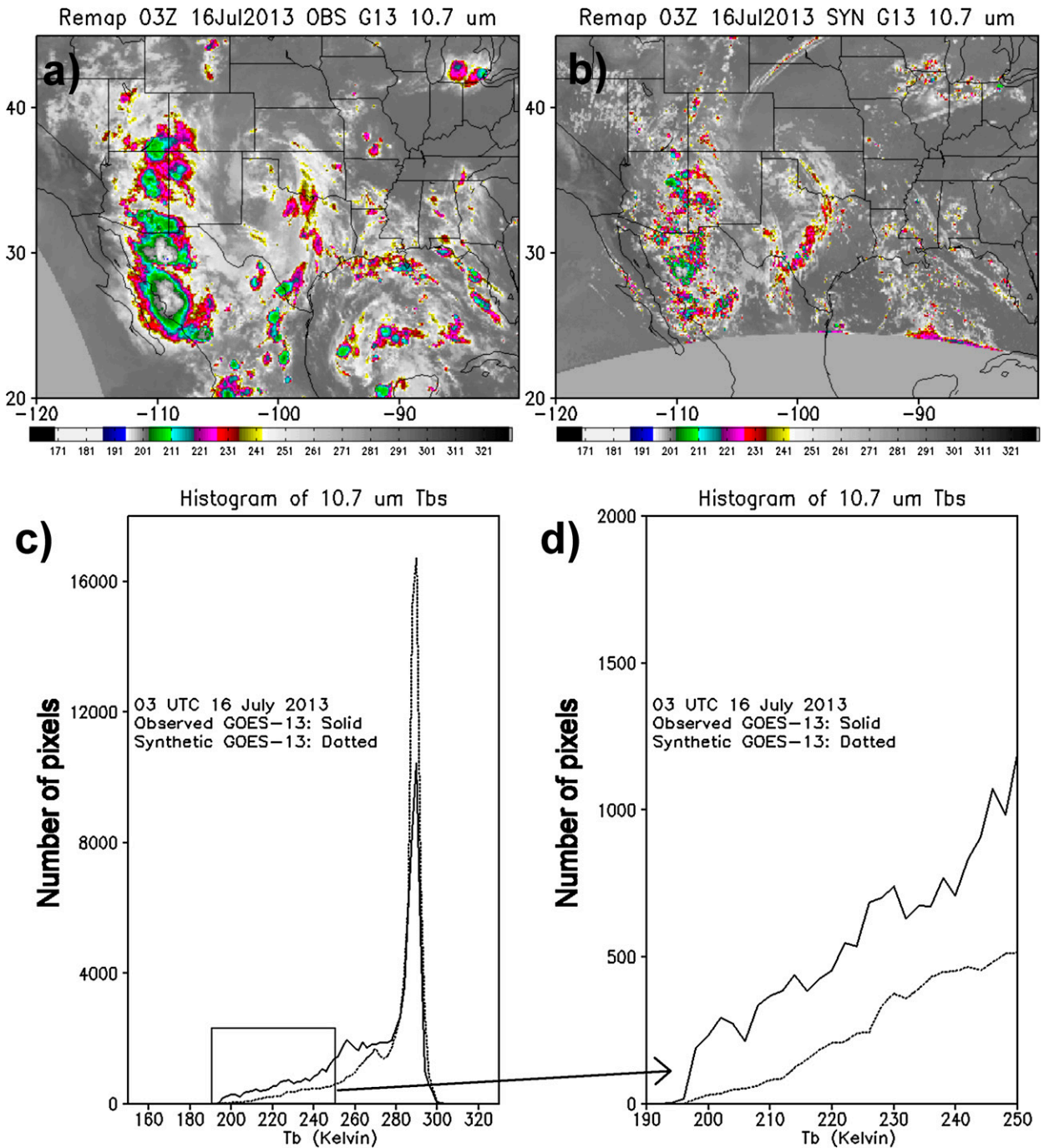
FIG. 4. As in Fig. 2, but valid at 0300 UTC 16 Jul 2013. The synthetic image is based on a 27-h forecast from the 4-km NSSL WRF.

a line located at the model grid point at $Y = 229$ bounded between model grid points $495 \leq X \leq 535$.

Figure 7a is a vertical cross section, along the line $Y = 229$ indicated in Fig. 6b, showing all five of the microphysical habits (g kg^{-1}), the 273-K freezing/melting level, and the 233-K homogeneous freezing level. Further, Fig. 7a illustrates the vertical orientation and pattern of habit types

through the convective updraft and simulated anvil of the storm in Fig. 6b. In addition, BTs along $Y = 229$ and $495 \leq X \leq 535$ are displayed in Fig. 7b. In particular, the locations of three relative minima can be identified in the BTs: $X = 519$, 514, and 507. A comparison of the brightness temperatures and mass mixing ratio of ice, snow, and graupel at these locations suggests the following: all three
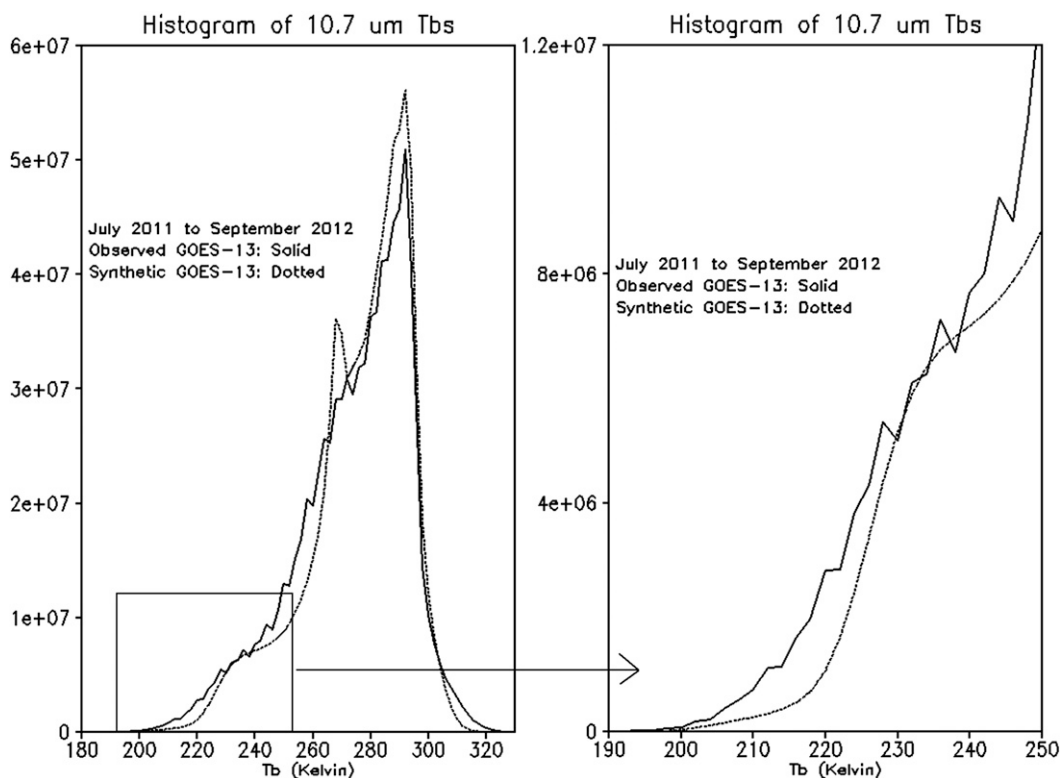
FIG. 5. Similar to the histograms in Figs. 2–4, but for all 9- to 36-h forecast images from July 2011 to September 2012.

BT minima occur at locations where the maxima of the mass mixing ratio of ice, snow, and graupel overlap at temperatures less than the homogeneous freezing temperature. In addition, a comparison of Figs. 7a,b suggest a mixing ratio of frozen mass in excess of about $0.5\,\mathrm{g\,kg^{-1}}$ in a simulated anvil could be sufficient for cloud top BT to match observations.

In general, anvils develop as a result of condensate transported by a convective updraft. As air accelerates upward from the boundary layer, cloud droplets form and are transported upward. Although cloud droplet mass can transfer into rain or snow, two dominant mass transfers of cloud droplets that occur within a simulated updraft are the conversion to graupel and ice. As suggested by Fig. 7a, values of cloud water mass mixing ratio decrease from about $2.0\,\mathrm{g\,kg^{-1}}$ to approximately $0.1\,\mathrm{g\,kg^{-1}}$ between the freezing/melting and homogeneous freezing level; while the remaining cloud droplet mass was converted into ice via homogeneous freezing. Homogeneous freezing of cloud droplets is the primary source of ice in a simulated anvil. One of the primary sinks of ice in the anvil was the conversion of ice to the snow category. In particular, values of ice mass outside the updraft were approximately $0.15\,\mathrm{g\,kg^{-1}}$ while those of snow were $1.5\,\mathrm{g\,kg^{-1}}$, an order of magnitude difference. As

a result of the nonzero fall speed of snow, mass was transported downward from the anvil by the snow field thereby removing ice condensate from the anvil region. An illustration of the conversions of habit types is shown in Fig. 8. Details of each microphysics process can be found in Hong and Lim (2006).

Based on results of the simulations discussed above and the pattern of the WSM6 habits in Fig. 7a, a possible reason for the lack of ice in the simulated anvil shown in Fig. 6b can be hypothesized. Too much cloud droplet mass was converted into graupel mass during ascent within the simulated updraft. An excessive mass transfer from cloud to graupel can reduce the amount of ice mass in the anvil that is produced during homogeneous freezing. Further, loss of ice results from mass conversion to snow within the anvil and laterally outside of the updraft. Snow hydrometeors subsequently precipitate out of the anvil. As a result, insufficient ice mass remains to expand the anvil laterally away from the overshooting dome. Precipitation settling of the larger particles was hypothesized by Van Weverberg et al. (2013). Sensitivity experiments were designed to explore the different conversion rates of the sources and sinks of cloud ice. These experiments represent a first step at diagnosing the loss of simulated ice in the upper troposphere.
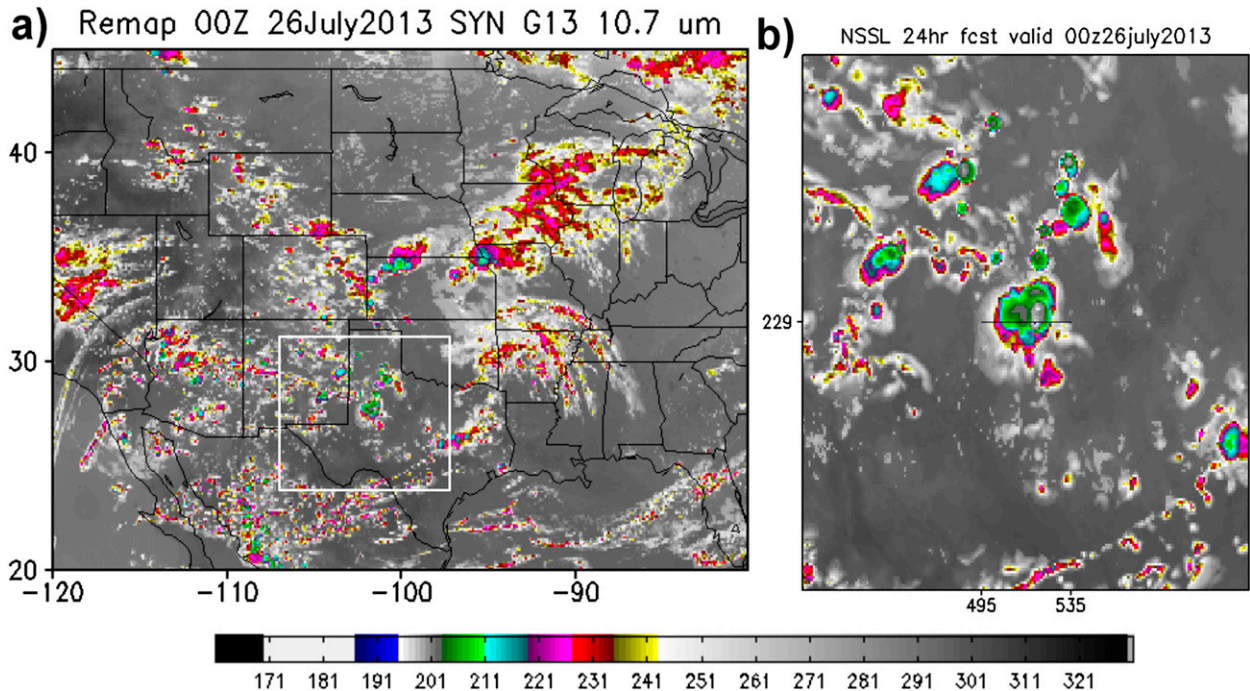
FIG. 6. Synthetic *GOES-13* image at 10.7 μm valid at 0000 UTC 26 Jul 2013 for (a) a remapped portion of the full domain and (b) zoomed over the white box shown in (a) over Texas, with the location of a vertical cross section along the line $Y = 229$, bounded between $495 \leq X \leq 535$.

5. Sensitivity experiments with WSM6

Similar to the experiments of Lim and Hong (2010), two-dimensional idealized thunderstorm simulations were conducted with WRF-ARW, version 3.5. In particular, a horizontal grid spacing of 1 km was used along with 80 vertical levels equally spaced at 250 m. Consequently, the model top was located at 20 km. As is typical with idealized thunderstorm simulations, an 8-km-wide warm thermal anomaly consisting of a 3-K maximum perturbation was used to trigger convection. Surface wind speeds of 12 m s^{-1} in the positive x direction decreased to 0.0 at an elevation of 2.5 km. Above 2.5 km, environmental winds were 0.0. Although a three-dimensional turbulent kinetic energy subgrid-scale scheme was used, most other types of physics parameterizations were turned off such as boundary layer physics and radiation.

These experiments were designed to examine the response of ice mass in a simulated anvil to changes of the conversion rates associated with cloud ice. A total of six conversions were reduced. They are 1) snow and/or graupel accretes cloud droplets [ps(g)acw], 2) self-aggregation of ice by ice to form snow (psaut), 3) graupel accretes ice to form graupel (pgaci), 4) snow accretes ice to form snow (psaci), 5) rain accretes ice to form snow or graupel (praci), and 6) sublimation of cloud ice to form vapor (pisub). As part of the conversions pgacw

and psacw, the mass-weighted terminal velocity suggested by Dudhia et al. (2008) was used for both the snow and graupel species. As a result, the conversion pgacw and psacw are calculated together; hence, ps(g)acw is used as a label for the conversion above. All six conversions are labeled in Fig. 8 along lines from cloud water to other hydrometeors (rain, graupel, and snow) and from cloud ice to graupel and snow.

A total of seven simulations were conducted each of which utilized one reduction factor that has a value of 50%. A control simulation, hereafter CNTL, was run in which no changes were made to any of the six conversion rates previously listed. In the first sensitivity experiment, hereafter SEN1, both conversions from cloud droplets to snow and graupel ps(g)acw were reduced by 50%. In the second and third sensitivity experiments, hereafter SEN2 and SEN3, aggregation of ice to snow, psaut, and accretion of ice by graupel, (pgaci), were both reduced by 50%, respectively. Similarly, in the fourth and fifth sensitivity experiments, denoted SEN4 and SEN5, accretion of ice by snow, (psaci), and accretion of ice by rain, (praci), were also reduced by 50%, respectively. In the last sensitivity experiment, SEN6, sublimation of ice, (pisub), was reduced by 50%. This last experiment was included because of the hypothesis by Van Weverberg et al. (2013) that sublimation of ice may be the cause of ice loss in the WSM6 routine. A value of 50% was
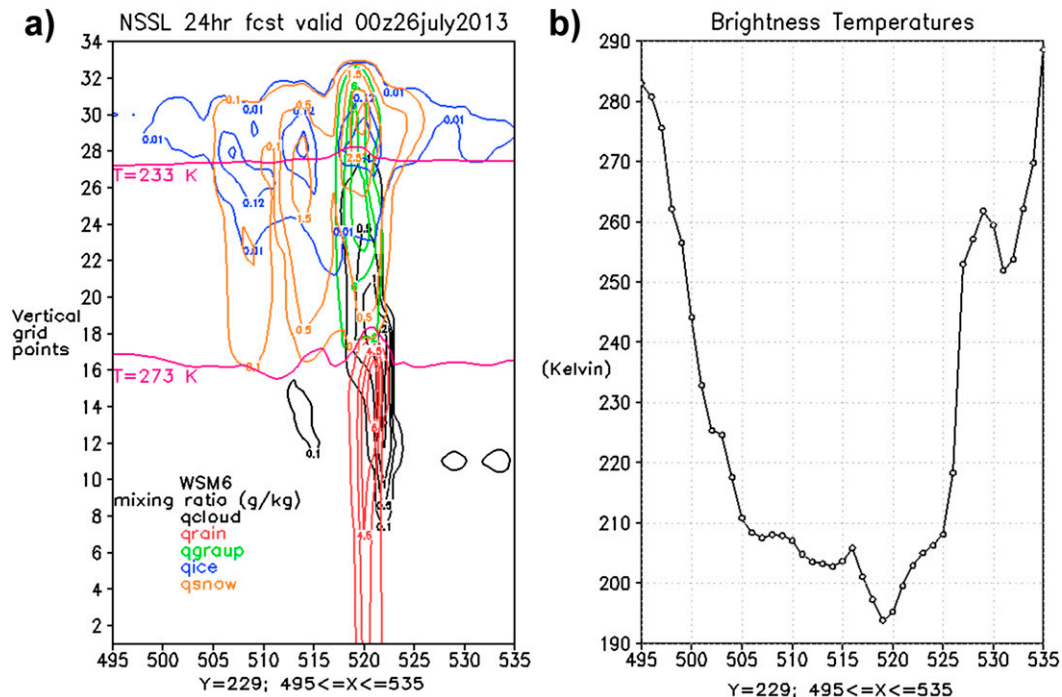
FIG. 7. (a) Vertical cross section taken along the line $Y = 229$, bounded between $495 \le X \le 535$ as indicated in Fig. 6b. All five WSM6 microphysical habits are contoured along with the freezing–melting and homogeneous freezing isotherms. To aid readability, contours of all hydrometeors are cloud water (0.1, 0.5, 1.0, 2.0); rain (1.0, 3.0, 4.5, 6.0); graupel (2.0, 6.0, 8.0); ice (0.01, 0.12, 0.20); and snow (0.1, 0.5, 1.5, 2.5, 3.0, 3.5), respectively. (b) Synthetic 10.35-μm brightness temperatures (K) along the line $Y = 229$.

chosen only as a means to demonstrate which conversions have the most significant influence on the ice mass. In all cases, a two-dimensional convective updraft was simulated over a 7-h period. During that time period, convection exhibited successive multicellular behavior. Consequently, results will be shown within the first 3.5 h of the simulation; a time period that was prior to the first instance of convective redevelopment.

To show changes in the results of the experiments, differences in spatial and temporal averages between the CNTL and any one of the sensitivity experiments were chosen for display in Fig. 9. Since cloud ice mass is the variable of interest, images in Fig. 9 display the 3.5-h average ice mass of the CNTL case subtracted from the 3.5-h average ice mass of a given sensitivity experiment. A suggestion of an increase in ice mass in the SEN1 is evident in Fig. 9a near the base of the ice field. A result that is consistent with a decrease of the conversion of cloud water to graupel and/or snow. Consequently, more cloud water mass is available to pass through the homogeneous freezing level. A reduction in the self-aggregation of ice to form snow resulted in a small change in the ice field in the SEN2 case (Fig. 9b). Likewise, a reduction in the conversion from cloud ice to graupel, SEN3, was unable to yield a significant increase in cloud ice as seen

in Fig. 9c. Similar remarks hold for the SEN5 experiment (Fig. 9e). Results from SEN6 are unable to support the hypothesis of Van Weverberg et al. (2013) that sublimation of ice is the cause of ice loss in the WSM6 routine. As is evident in Fig. 9d, a reduction in the accretion of ice by snow to form snow leads to a significant increase in ice compared to not only the CNTL experiment, but also compared to any of the other sensitivity experiments.

Results of the sensitivity experiments suggest which conversions could be reformulated. Since cloud droplet mass is the main source of ice in a simulated anvil, the conversions to graupel or snow could be altered to ensure sufficient liquid water mass passes through the homogeneous freezing level. Results from the SEN4 experiment suggest that accretion of ice by snow represented a significant loss of anvil ice mass. As a result, the sink of ice to snow could be reduced significantly. As shown in SEN2, the loss of ice mass due to self-aggregation of ice within an anvil is not significant. However, self-aggregation of ice is potentially important because such a process initiates the increase of snow mass, from which the dominant process of accretion of ice by snow occurs. Lim and Hong (2012) analyzed the cloud microphysical budget in the WDM6 scheme during the
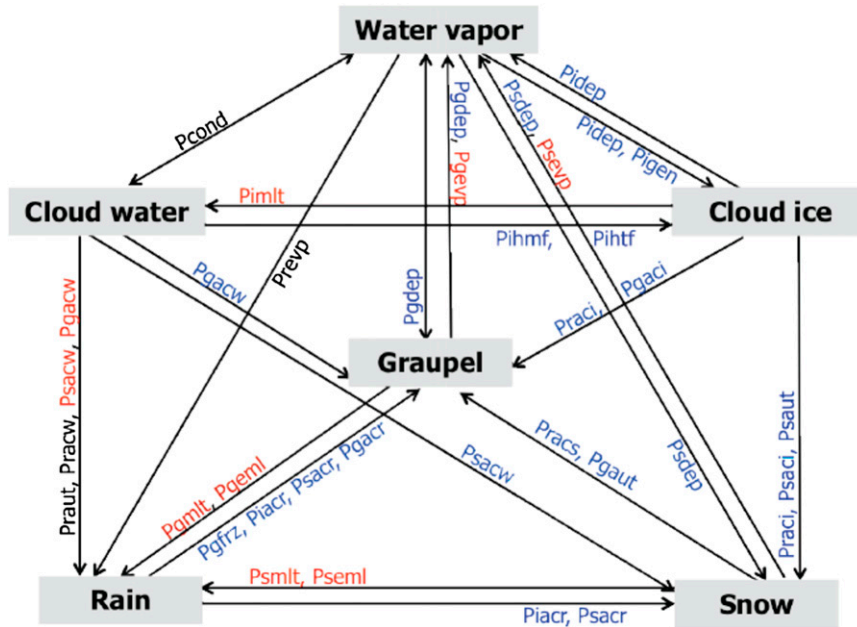
FIG. 8. Schematic of sources and sinks for each of the five microphysical habit types and water vapor in the WSM6 microphysical parameterization. The terms in red (blue) are activated when the temperature is above (below) 0°C, whereas the terms in black are activated when the temperature is either above or below 0°C.

summer convective rainfall period over Korea and showed that the accretion of ice by snow is the most efficient sink of cloud ice among the microphysics processes. Results from SEN4 suggest that accretion of ice by snow is not only a dominant process, but may be too excessive. Hence, a significant loss of ice mass from a simulated anvil results from precipitation settling of snow.

Although snow may have a relatively large terminal fall speed, a reduction of the accretion process of ice to snow has the potential to increase ice mass and thus result in a more realistic simulated anvil. Further, as implied by Van Weverberg et al. (2013), the terminal fall speed of snow could be reduced. A reduction in precipitation settling could also result in more condensate mass (snow plus ice) in a simulated anvil.

A few cautious remarks about the physical interpretation of each panel in Fig. 9 are warranted. As stated earlier, each panel in Fig. 9 is different from an instantaneous difference between any one sensitivity experiment and the control case. Slight shifts in the location of a given sensitivity storm compared to the control storm, the temporally unsteady behavior of a given sensitivity storm compared to the control storm, temporal averaging, and the microphysical modifications are all contained in Fig. 9. Results in Fig. 9d suggest a 50% reduction of psaci should be the process to test in a three-dimensional setting since they stood out against

the other conversions as the one with the greatest increase, over most of the anvil, over most of the history of the storm.

To further support the claim that a reduction of the accretion of ice by snow will lead to a more realistic ice field, the three-dimensional experiment shown in Fig. 6 was repeated. In the new experiment, a change was made to the WSM6 package to reduce psaci by 50%; results are shown in Fig. 10. Synthetic *GOES-13* images at 10.7 μm are shown together as a way to compare the original simulation (Fig. 10a) with the new results (Fig. 10b). An examination of the two images shows an increase in cold pixels, suggesting a corresponding increase in cloud ice in many areas of the new simulation. Quantification of the difference was done by the use of histograms for both simulations as is shown in Fig. 11. As expected, with more cloud ice there should be fewer warmer pixels in the new case. Such an expectation is supported by a shift of the histogram of the new case (dotted red contour) to the left of the histogram of the original case (dotted black contour) in Fig. 11a at temperatures at and above 300 K. Further, a closer view of the histogram at colder temperatures (Fig. 11b) reveals additional cold pixels in the new image compared to the original image. Thus, as shown in the figure, a 50% reduction in psaci yielded an improvement of the synthetic image (dotted red contour) compared to observations (solid contour).
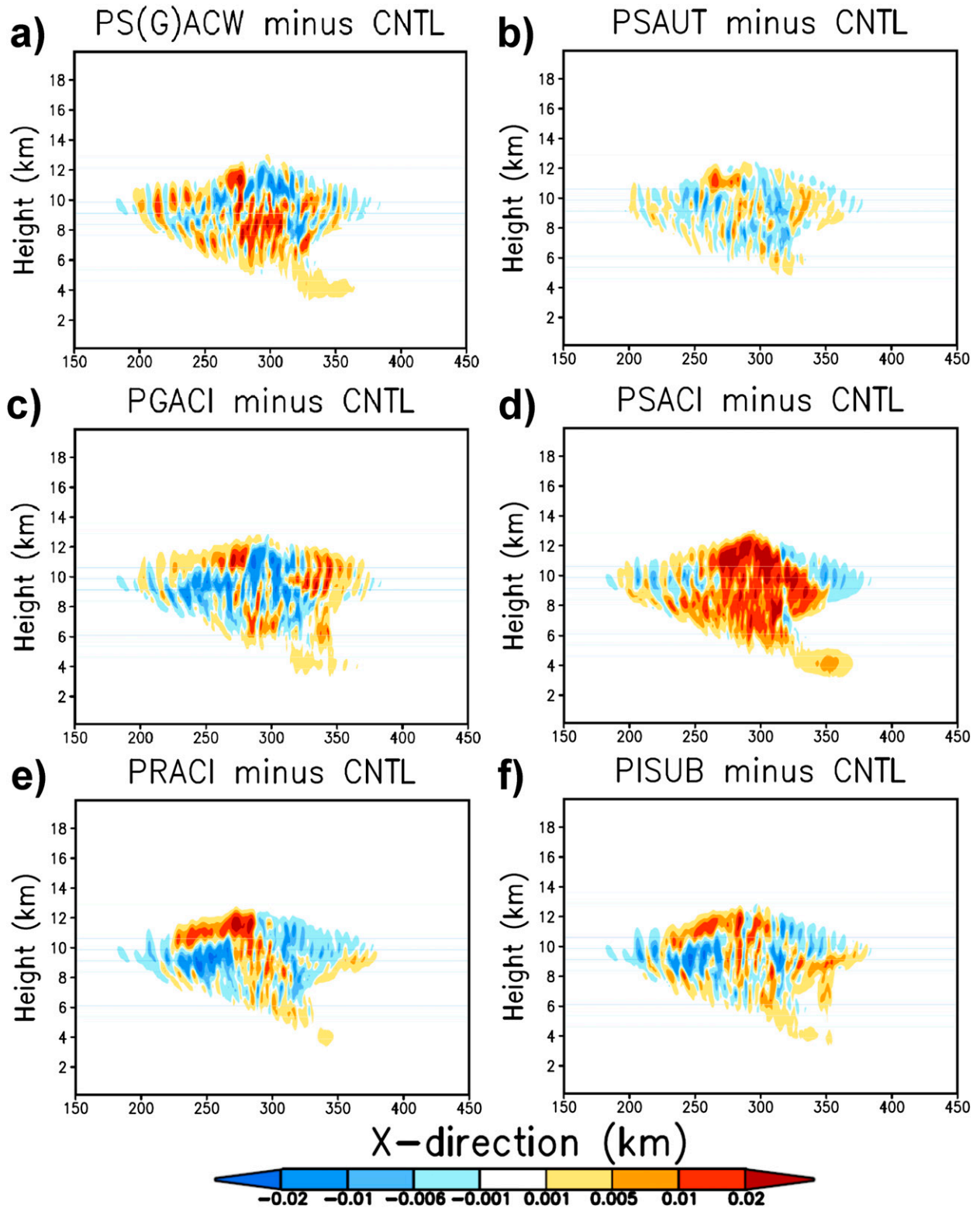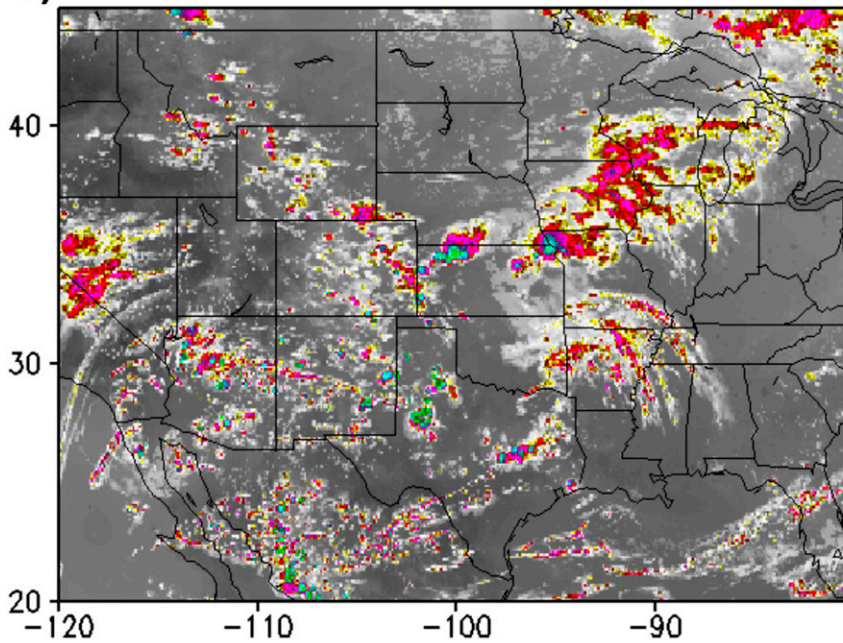
FIG. 9. Differences in time-averaged mass mixing ratio (g kg^{-1}) of cloud ice for (a) SEN1, (b) SEN2, (c) SEN3, (d) SEN4, (e) SEN5, and (f) SEN6, all − CNTL.

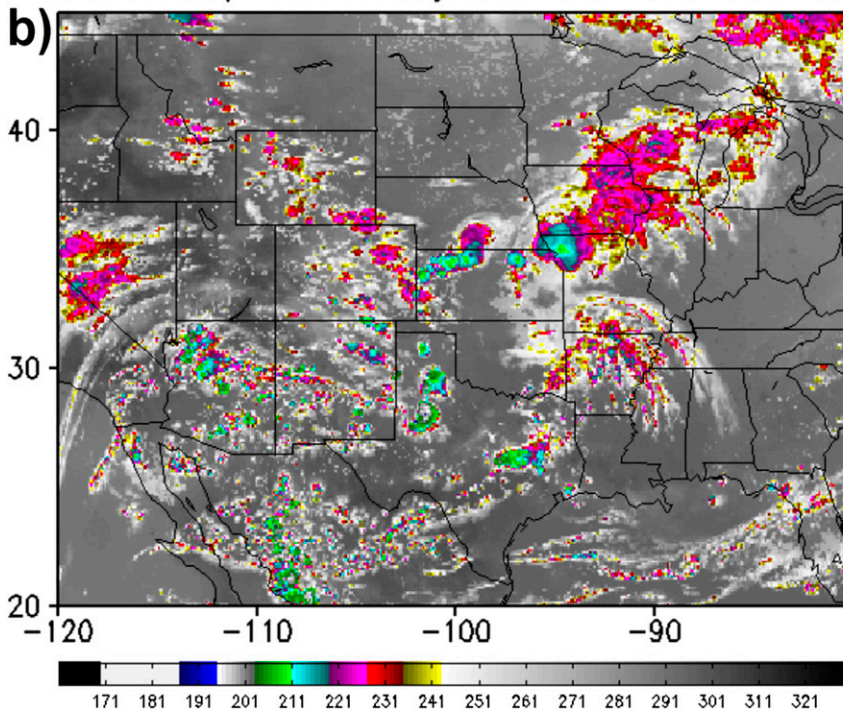FIG. 10. Synthetic *GOES-13* image at 10.7 μm valid at 0000 UTC 26 Jul 2013 for (a) the original 100% psaci run as seen in Fig. 6a and (b) a new run with 50% psaci.
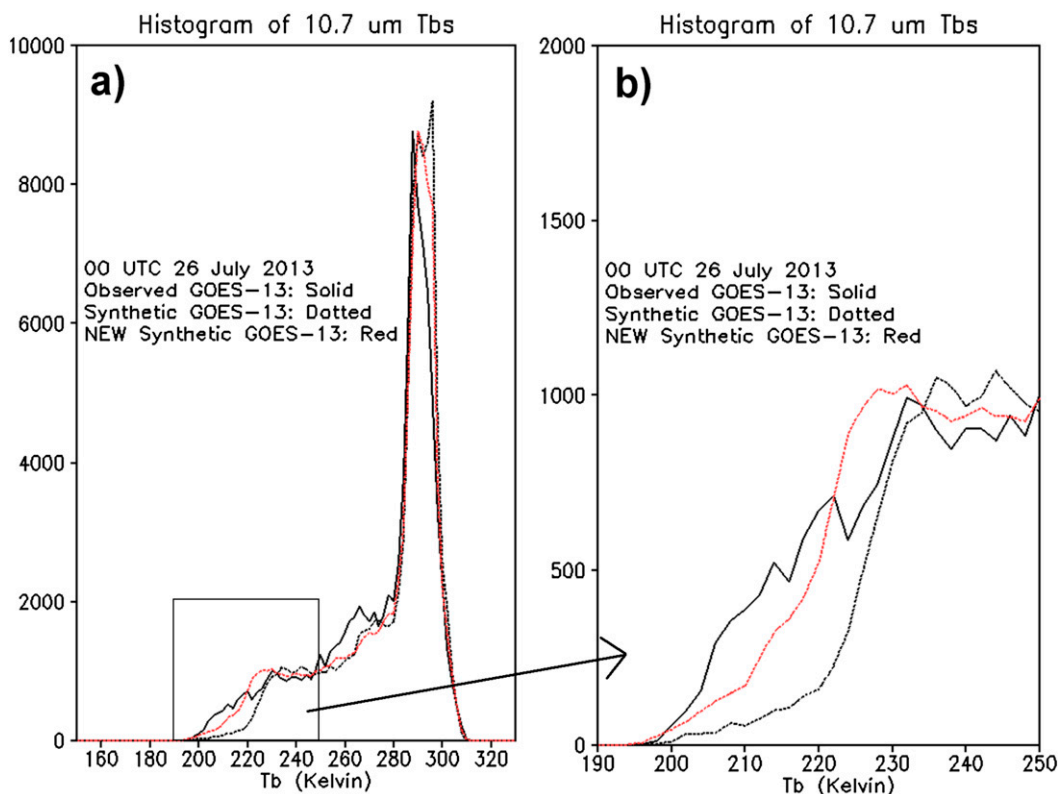
FIG. 11. Histograms of the synthetic *GOES-13* images shown in Fig. 10 and observed *GOES-13*. Observed data are indicated by a solid black contour; the dotted black contour represents data from the original simulation while the red dotted contour represent data from the new simulation. Brightness temperatures (a) from 160 to 320 K and (b) from 190 to 250 K.

6. Summary and conclusions

Over the past several years, there have been improvements in the generation of synthetic satellite imagery of numerical model output. Recent efforts have focused on the evaluation of simulated cloud fields in a variety of numerical models. Evaluations are typically done by comparing synthetic imagery to observed imagery by means of statistical techniques. Should a discrepancy in the synthetic imagery be identified, then such information can be used, for example, to improve microphysical routines. Synthetic imagery from the 4-km NSSL WRF-ARW has been used to identify strengths and weaknesses of the many microphysical routines in this model. One microphysical routine has been identified as having a consistent weakness: WSM6. A comparison between synthetic imagery and observed imagery has revealed that the WSM6 package produces too little ice mass in the upper troposphere. For clarity, results of this study do not imply that the WSM6 routine is the only microphysics parameterization that has weaknesses.

Forecasters from the SPC and other National Weather Service offices use the 4-km NSSL WRF-ARW model for guidance on thunderstorm forecasts. As such, any weaknesses that can be identified in simulated cloud fields associated with convection should be addressed so that subsequent improvements to the WSM6 microphysics will improve the model forecasts. Statistical analysis of synthetic imagery from the NSSL WRF-ARW consistently highlighted the lack of upper-tropospheric ice compared to observations. In particular, specific examples of side-by-side comparisons between synthetic and observed *GOES-13* imagery at 10.7 μm were provided. These examples showed a significant reduction of simulated anvil coverage during the 2013 convective season. A separate simulation was then used to show the vertical distribution of habit types through a convective updraft.

Vertical plots of microphysical species are useful in identifying potential shortcomings. In the case of the 25 July 2013 simulation, small amounts of ice mass were evident in the anvil. Several processes were examined that might explain the low bias in anvil ice. Cloud droplet mass decreased significantly in the vertical prior

to reaching the level of homogeneous freezing, and significant amounts of snow mass existed at the base of and below the anvil. These patterns suggested that too much cloud droplet mass was being converted into graupel, leaving little cloud droplet mass to pass through the homogeneous freezing level as a source of ice in the anvil. In addition, too much ice mass was converted into snow. Because of the relatively large terminal fall speed of snow, too much frozen water mass descended from the simulated anvil. In other words, instead of cloud ice spreading horizontally to form a realistic anvil canopy, significant amounts of cloud ice were converted into snow that subsequently descended.

Sensitivity simulations suggested which microphysical processes in the WSM6 package could be reformulated. A 50% reduction in the transfer of cloud droplets to graupel had a small positive impact on anvil ice amounts. In contrast, a noticeable increase in anvil ice mass occurred when accretion of ice by snow was reduced. Although the aggregation of ice to form snow is a relatively minor process in removing cloud ice, this process is the main mechanism for snow to form. Once snow has formed, the accretion of ice by snow is quite efficient at removing ice mass from a simulated anvil. Therefore, reducing the accretion of ice by snow can result in more ice mass in an anvil despite the larger fall speed of snow. An additional test was conducted in which a 50% reduction of only the accretion of ice by snow was included in the 3D case of 25 July 2013. Results from this test also indicated a significant increase in upper-level cloud ice when compared to the original simulation and observations. These sensitivity experiments represented a first step at identifying the conversion rate that is too excessive at removing ice mass from the ice field. As such, these conversions can be reformulated in a more physically realistic manner compared to the idealized 50% reduction.

The goal of this paper was to identify a possible shortcoming in the WSM6 microphysical scheme. Future work involves a more careful examination of both the WSM6 and WDM6 microphysical packages using full three-dimensional model simulations. Comparisons between simulated anvil clouds and observed anvil clouds should be used to help adjust the conversion rates between various hydrometeor species.

REFERENCES

Bikos, D., and Coauthors, 2012: Synthetic satellite imagery for real-time high-resolution model evaluation. *Wea. Forecasting,* **27,** 784–795, doi:10.1175/WAF-D-11-00130.1.

Bryan, G. H., and H. Morrison, 2012: Sensitivity of a simulated squall line to horizontal resolution and parameterization of microphysics. *Mon. Wea. Rev.,* **140,** 202–225, doi:10.1175/MWR-D-11-00046.1.

Cintineo, R., J. A. Otkin, M. Xue, and F. Kong, 2014: Evaluating the performance of planetary boundary layer and cloud microphysical parameterization schemes in convection-permitting ensemble forecasts using synthetic *GOES-13* satellite observations. *Mon. Wea. Rev.,* **142,** 163–182, doi:10.1175/MWR-D-13-00143.1.

Clark, A. J., and Coauthors, 2012: An overview of the 2010 Hazardous Weather Testbed Experimental Forecast Program Spring Experiment. *Bull. Amer. Meteor. Soc.,* **93,** 55–74, doi:10.1175/BAMS-D-11-00040.1.

——, R. G. Bullock, T. L. Jensen, M. Xue, and F. Kong, 2014: Application of object-based time-domain diagnostics for tracking precipitation systems in convection-allowing models. *Wea. Forecasting,* **29,** 517–542, doi:10.1175/WAF-D-13-00098.1.

Cotton, W. R., and Coauthors, 2003: RAMS 2001: Current status and future direction. *Meteor. Atmos. Phys.,* **82,** 5–29, doi:10.1007/s00703-001-0584-9.

Dudhia, J., S.-Y. Hong, and K.-S. Lim, 2008: A new method for representing mixed-phase particle fall speeds in bulk microphysics parameterizations. *J. Meteor. Soc. Japan,* **86A,** 33–44, doi:10.2151/jmsj.86A.33.

Goodman, S. J., and Coauthors, 2012: The GOES-R Proving Ground: Accelerating user readiness for the Next-Generation Geostationary Environmental Satellite System. *Bull. Amer. Meteor. Soc.,* **93,** 1029–1040, doi:10.1175/BAMS-D-11-00175.1.

Grasso, L. D., and T. Greenwald, 2004: Analysis of 10.7-μm brightness temperatures of a simulated thunderstorm with two-moment microphysics. *Mon. Wea. Rev.,* **132,** 815–825, doi:10.1175/1520-0493(2004)132<0815:AOMBTO>2.0.CO;2.

——, and D. Lindsey, 2011: An example of the use of synthetic 3.9 μm *GOES-12* imagery for two-moment microphysical evaluation. *Int. J. Remote Sens.,* **32,** 2337–2350, doi:10.1080/01431161003698294.

——, M. Sengupta, and M. DeMaria, 2010: Comparison between observed and synthetic 6.5 and 10.7 μm *GOES-12* imagery of thunderstorms that occurred on 8 May 2003. *Int. J. Remote Sens.,* **31,** 647–663, doi:10.1080/01431160902894483.

Hong, S.-Y., and J.-O. J. Lim, 2006: The WRF single-moment 6-class microphysics scheme (WSM6). *J. Korean Meteor. Soc.,* **42,** 129–151.

Jankov, I., and Coauthors, 2011: An evaluation of five WRF-ARW microphysics schemes using synthetic GOES imagery for an atmospheric river event affecting the California coast. *J. Hydrometeor.,* **12,** 618–633, doi:10.1175/2010JHM1282.1.

Jung, Y., M. Xue, and M. Tong, 2012: Ensemble Kalman filter analyses of the 29–30 May 2004 Oklahoma tornadic thunderstorm using one- and two-moment bulk microphysics schemes, with verification against polarimetric radar data. *Mon. Wea. Rev.,* **140,** 1457–1475, doi:10.1175/MWR-D-11-00032.1.

Kain, J. S., S. J. Weiss, J. J. Levit, M. E. Baldwin, and D. R. Bright, 2006: Examination of convection-allowing configurations of the WRF model for the prediction of severe convective weather: The SPC/NSSL Spring Program 2004. *Wea. Forecasting,* **21,** 167–181, doi:10.1175/WAF906.1.

——, S. R. Dembek, S. J. Weiss, J. L. Case, J. J. Levit, and R. A. Sobash, 2010: Extracting unique information from high-resolution forecast models: Monitoring selected fields and phenomena every time step. *Wea. Forecasting,* **25,** 1536–1542, doi:10.1175/2010WAF2222430.1.

Kong, F., and Coauthors, 2007: Preliminary analysis on the real-time storm-scale ensemble forecasts produced as part of the NOAA hazardous weather testbed 2007 spring experiment. *22nd Conf. on Weather Analysis and Forecasting/18th Conf. on Numerical Weather Prediction,* Salt Lake City, UT, Amer. Meteor. Soc., 3B.2. [Available online at https://ams.confex.com/ams/22WAF18NWP/techprogram/paper_124667.htm.]

Lazzara, M. A., and Coauthors, 1999: The Man computer Interactive Data Access System: 25 years of interactive processing. *Bull. Amer. Meteor. Soc.,* **80,** 271–284, doi:10.1175/1520-0477(1999)080<0271:TMCIDA>2.0.CO;2.

Lim, K.-S. S., and S.-Y. Hong, 2010: Development of an effective double-moment cloud microphysics scheme with prognostic cloud condensation nuclei (CCN) for weather and climate models. *Mon. Wea. Rev.,* **138,** 1587–1612, doi:10.1175/2009MWR2968.1.

——, and ——, 2012: Investigation of aerosol indirect effects on simulated flash-flood heavy rainfall over Korea. *Meteor. Atmos. Phys.,* **118,** 199–214, doi:10.1007/s00703-012-0216-6.

Lin, Y.-L., R. D. Farley, and H. D. Orville, 1983: Bulk scheme of the snow field in a cloud model. *J. Climate Appl. Meteor.,* **22,** 1065–1092, doi:10.1175/1520-0450(1983)022<1065:BPOTSF>2.0.CO;2.

Mellor, G. L., and T. Yamada, 1982: Development of a turbulence closure model for geophysical fluid problems. *Rev. Geophys.,* **20,** 851–875, doi:10.1029/RG020i004p00851.

Oberthaler, A. J., and P. M. Markowski, 2013: A numerical simulation study of the effects of anvil shading on quasi-linear

convective systems. *J. Atmos. Sci.,* **70,** 767–793, doi:10.1175/JAS-D-12-0123.1.

Otkin, J. A., T. J. Greenwald, J. Sieglaff, and H.-L. Huang, 2009: Validation of a large-scale high-resolution WRF model simulation using SEVIRI satellite observations. *J. Appl. Meteor. Climatol.,* **48,** 1613–1626, doi:10.1175/2009JAMC2142.1.

Rutledge, S. A., and P. V. Hobbs, 1984: The mesoscale and microscale structure and organization of clouds and precipitation in midlatitude cyclones. XII: A diagnostic modeling study of precipitation development in narrow cold-frontal rainbands. *J. Atmos. Sci.,* **41,** 2949–2972, doi:10.1175/1520-0469(1984)041<2949:TMAMSA>2.0.CO;2.

Seemann, S. W., E. E. Borbas, R. O. Knuteson, G. R. Stephenson, and H.-L. Huang, 2008: Development of a global infrared land surface emissivity database for application to clear sky sounding retrievals from multispectral satellite radiance measurements. *J. Appl. Meteor. Climatol.,* **47,** 108–123, doi:10.1175/2007JAMC1590.1.

Skamarock, W. C., J. B. Klemp, J. Dudhia, D. O. Gill, D. M. Barker, W. Wang, and J. G. Powers, 2005: A description of the advanced research WRF version 2. NCAR Tech. Note NCAR/TN-468+STR, 88 pp. [Available online at http://www.mmm.ucar.edu/wrf/users/docs/arw_v2.pdf.]

Thompson, G., P. R. Field, R. M. Rasmussen, and W. D. Hall, 2008: Explicit forecasts of winter precipitation using an improved bulk microphysics scheme. Part II: Implementation of a new snow parameterization. *Mon. Wea. Rev.,* **136,** 5095–5115, doi:10.1175/2008MWR2387.1.

Van Weverberg, K., and Coauthors, 2013: The role of cloud microphysics parameterization in the simulation of mesoscale convective system clouds and precipitation in the tropical western Pacific. *J. Atmos. Sci.,* **70,** 1104–1128, doi:10.1175/JAS-D-12-0104.1.

Xue, M., and Coauthors, 2007: CAPS realtime storm-scale ensemble and high-resolution forecast as part of the NOAA Hazardous Weather Testbed 2007 spring experiment. *22nd Conf. on Weather Analysis and Forecasting/18th Conf. on Numerical Weather Prediction,* Salt Lake City, UT, Amer. Meteor. Soc., 3B.1. [Available online at https://ams.confex.com/ams/22WAF18NWP/techprogram/paper_124587.htm.]